

# NUMERICAL SIMULATION OF THE RESPONSE CHARACTERISTICS OF THE WING STRUCTURE OF A SEAPLANE PLANING IN WAVE

Zhiwei Lu<sup>1</sup>, Yanghui Li<sup>1,2</sup>, Jichang Chen<sup>1</sup>, Mingbo Tong<sup>1</sup> & Bin Wu<sup>1,3</sup>

<sup>1</sup>College of Aerospace Engineering, Nanjing University of Aeronautics and Astronautics, Nanjing 210016, China <sup>2</sup>Marine Design and Research Institute of China, Shanghai 200011, China <sup>3</sup>Key Aviation Scientific and Technological Laboratory of High-Speed Hydrodynamic, China Special Vehicle Research Institute, Jingmen 448035, China

#### **Abstract**

The working environment and working objectives of seaplanes are relatively special, and they need to complete the water takeoff and landing process at a high frequency. Seaplanes often come into contact with waves during the taxiing stage, and the attitude angle and heave state of the seaplane oscillate violently. The larger aspect ratio of large seaplanes improves the lift-to-drag ratio while also reducing the overall stiffness of the wing. When the fuselage is subjected to a large vertical overload, the high-frequency vibration of the wing structure poses a hidden danger to the safety of the seaplane. Therefore, this paper uses numerical simulation methods to study and analyze the motion response and wing structure response characteristics of large seaplanes during planing.

**Keywords:** two phase flow, seaplane, fluid structure coupling, 6-DOF, structure vibration

#### 1. Introduction

As a special surface transportation tool, surface aircraft has many advantages over conventional aircraft and offshore mobile platforms due to its unique structural characteristics and flight mode: it can take off and land on the sea, has high flight speed, good safety, good economy, and strong multipurpose capabilities. It can be widely used in landing operations, personnel and cargo transportation on islands and reefs and offshore oil and gas platforms, search and rescue, emergency medical care and many other fields.

The take-off/landing conditions of surface aircraft are complex. They not only need to complete take-off/landing on land, but also need to complete related take-off/landing tasks on the water surface. Therefore, it is necessary to study the hydroplaning characteristics of aircraft under complex sea conditions and at different flight speeds. However, these water loads often have strong nonlinear characteristics and are difficult to estimate through engineering. At present, they are often measured through pool tests, which requires a lot of manpower and financial resources. However, most of the test simulations are hydroplaning on calm water surfaces and hydroplaning with small regular waves, while the real sea surface environment is high sea conditions and irregular waves. It is difficult to simulate the test and has limitations. Through numerical simulation, the overall hydroplaning performance of the aircraft, as well as the overload and bottom pressure of the aircraft during hydroplaning can be studied. The flight safety of surface aircraft under complex sea conditions can be evaluated, the safety and reliability of the aircraft during hydroplaning can be ensured, and the design cost and design cycle can be reduced. It has important guiding significance and practical value for the design of surface aircraft.

The hydroplaning characteristics of seaplanes directly affect their ability to take off and land on the water. In order to ensure safety during take-off and landing, seaplanes need to have good stability during the gliding process. Since seaplanes are subject to the combined effects of aerodynamics and hydrodynamics when gliding on the water, and the movement involves technical issues such as

multiphase flow, the six-degree-of-freedom motion of the entire aircraft, and the capture of the waterair interface, the hydroplaning problem of seaplanes has been widely studied in three dimensions: theory, experiment, and numerical calculation.

The results of seaplane towing tests are highly reliable, but the test cycle is long, the cost is high, and usually only a scaled model can be used for testing. This series of shortcomings, coupled with the improvement of computer computing level and the development and improvement of computational fluid dynamics theory in recent years, numerical simulation has gradually become the mainstream method for solving the problems of seaplane take-off, landing and planing on the water surface. In 2019, Shao [1] conducted a computational study on the resistance of a planing boat based on the commercial software STAR-CCM+, focusing on the influence of the time step and the processing of near-wall grids on the calculation accuracy of the planing boat resistance, and proposed a method to improve the accuracy of CFD solutions for such problems. In 2018, Cai [2] of the Special Flight Institute studied the gliding process of a tandem-wing amphibious aircraft on a static water surface by numerical simulation. The volume fraction method (VOF) and the overlapping grid method were used to effectively capture the large-scale motion flow field of a tandem-wing amphibious aircraft during planing. In 2019, Duan [3] used the blade-disk method to simulate propeller slipstream based on the OpenFOAM platform, and conducted a numerical analysis of the dolphin motion of a seaplane when gliding on the water surface at high speed.

They also proposed a stable boundary for the aircraft during gliding and a rudder deflection scheme to improve the gliding posture motion. In 2020, Zhao [4] conducted a numerical simulation of the sixdegree-of-freedom motion state of a seaplane during landing and gliding based on the commercial software Fluent, verifying the good adaptability of the overall dynamic mesh during the landing and gliding of the seaplane on the water surface. Agostino De Marco [5] used the large eddy simulation (LES) method to analyze and compare the advantages and disadvantages of overlapping meshes and deformed meshes when calculating the gliding of a gliding body with a step, and conducted a numerical analysis of the air splashes on both sides of the step and the complex three-dimensional vortex behind the step. The numerical simulation results obtained are in good agreement with the experimental data, and the vortex system obtained is similar to the manifold observed in the drag experiment, which fully proves that CFD technology has high accuracy in solving high-speed water surface gliding problems. Garland and Maki [6] studied the lift-to-drag ratio of a two-dimensional planing surface using a numerical method. The results showed that the position of the steps on the planing surface significantly affected the lift-to-drag ratio of the planing body during gliding. Matveev [7] studied a two-dimensional planing surface with steps using the hydrodynamic discrete source method and numerically calculated the water surface changes during gliding, the wetted area of the bottom of the ship the pressure coefficient and the Froude number at a specific location. In another study by Matveev, the linearized potential flow theory was used to numerically analyze the steady half-molded hull and the pressure distribution in the selected area and the cavity calculation results were given [8]. Lotfi [9] used ANSYS-CFX to analyze the motion characteristics of the planing body by solving the unsteady Reynolds-averaged Navier-Stokes equations and combining the fluid volume fraction method. Stern [10] used a similar method to numerically calculate and analyze the drag reduction effect of the air cushion during gliding, and numerically calculated and evaluated the free surface capture, turbulence model construction, six-degree-of-freedom motion prediction, dynamic overlapping grids, and local grid adaptive refinement.

#### 2. Numerical Solution Methods

This study analyzes the wing structural response during seaplane planing. The physical process is very complex, and theoretical analysis obviously cannot solve this problem. The towing test of the scaled model physical pool is difficult to simultaneously meet the similarity of the planing Froude number (Fr) and the Reynolds number (Re), and it is also difficult to ensure that the wing structural characteristics are still of reference value after scaling. Therefore, numerical methods based on computational fluid dynamics and computational solid mechanics have become the most effective means to solve such problems.

## 2.1 Computational fluid dynamics governing equations

The movement of fluids needs to follow three conservation laws, namely the law of conservation of mass, the law of conservation of momentum, and the law of conservation of energy. Considering that the Mach number of the object of this study is small, there is no need to consider the solution of the energy equation in the numerical calculation. The law of conservation of mass is reflected in the control equation, which is the continuity equation. Its essence is that the change in mass in the control body per unit time is equal to the mass flow rate in and out of the control body surface. The integral form of the continuity equation is:

$$\frac{\partial}{\partial t} \iiint_{\Omega} \rho d\Omega + \iint_{S} \rho \overrightarrow{V} \cdot d\overrightarrow{S} = 0 \tag{1}$$

According to the divergence theorem, the integral form of the continuity equation can be transformed into differential form:

$$\frac{\partial \rho}{\partial t} + \nabla \cdot \left( \rho \vec{V} \right) = 0 \tag{2}$$

Wherein  $\rho$  represents the fluid density,  $\vec{V}$  represents the fluid velocity vector,  $\Omega$  is the control volume, S and is the surface of the control volume.

## 2.2 Structural response equations

This paper studies the situation when a seaplane is gliding, and the wing position undergoes structural deformation, while the rest of the parts maintain rigid motion. When all degrees of freedom of motion are released, the rigid body motion is controlled by two sets of motion equations, namely the translational momentum equations and the angular momentum equations. Their vector form is as follows: Translational momentum equations:

$$\frac{d(m_B \overrightarrow{v_C})}{dt} = \overrightarrow{F_B} \tag{3}$$

The angular momentum equations are:

$$\frac{d(I_C\overrightarrow{w_B})}{dt} = \overrightarrow{M_C} \tag{4}$$

Where  $m_B$  is the mass of the structure,  $\overrightarrow{v_C}$  is the velocity at the center of mass of the object,  $I_C$  is the moment of inertia tensor of the object,  $\overrightarrow{w_B}$  is the angular velocity,  $\overrightarrow{M_C}$  and  $\overrightarrow{F_B}$  is the force and moment acting on the structure. The force acting on the rigid body consists of two parts, one is the shear stress and pressure of the fluid load acting on the surface, and the other is the body force acting on the rigid body by gravity. Therefore, the load acting on the rigid body can be obtained by appropriate integration:

$$\overrightarrow{F_B} = \int_{S} (\overrightarrow{T} - p \overrightarrow{n}) dS + m_B \overrightarrow{g}$$
 (5)

$$\overrightarrow{M_C} = \int\limits_{S} (\overrightarrow{r} - \overrightarrow{r_C}) \times (\overrightarrow{T} - p\overrightarrow{n}) dS$$
 (6)

Among them,  $\overrightarrow{g}$  is the gravitational acceleration vector, and  $\overrightarrow{r}$  represents the relative position vector relative to the fixed reference frame.

### 3. Numerical Methods and Examples

## 3.1 Numerical wave generation verification

The waves involved in this article are all fifth-order Stokes waves. In fluid mechanics, Stokes waves are nonlinear, periodic, inviscid surface waves with a constant average depth. In the study adopts the velocity inlet wave generation method. Based on the above wave theory, the fifth-order Stokes wave is simulated in STAR CCM+ software, and the turbulence model is the  $k-\omega$  SST model. The wave parameters are wavelength L=6m, wave height H=0.2m, and water depth 1m.

The computational domain length of the numerical pool is five times the wavelength, a total of 30m; the area 1L away from the pressure outlet is set as the wave-breaking zone. The computational domain size and boundary condition settings are shown in Figure 1. In order to ensure accurate capture of waves, the wave position grid is adaptively encrypted, and the encryption level is 1, so that the encrypted grid size is L/140 in the wavelength direction and H/30 in the wave height direction. The adaptively encrypted grid is shown in Figure 1, and the overall grid volume is about 68,000. The boundary conditions and initial phases are shown in Figure 2. An entrance position P1 is set in the calculation domain, and four points P2, twice the wavelength, P3, and three times the wavelength away from the entrance position are used to monitor the wave morphology.

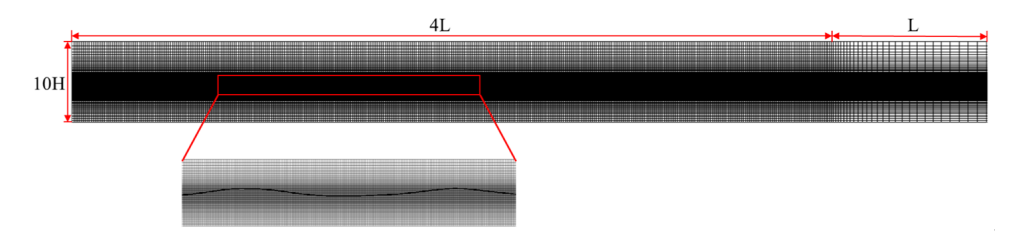


Figure 1 – Computational domain size and mesh division

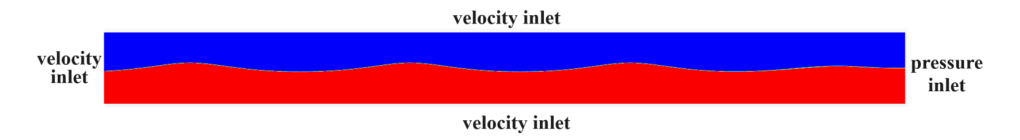


Figure 2 - Boundary conditions and initial phase

The calculated waveform is compared with the theoretical waveform. Figure 3-6 shows the waveform comparison of four station positions. The results show that the waveform obtained by adaptive grid encryption technology can match the theoretical waveform well. Whether it is the motion period or the motion amplitude, the numerical simulation results can capture it well.

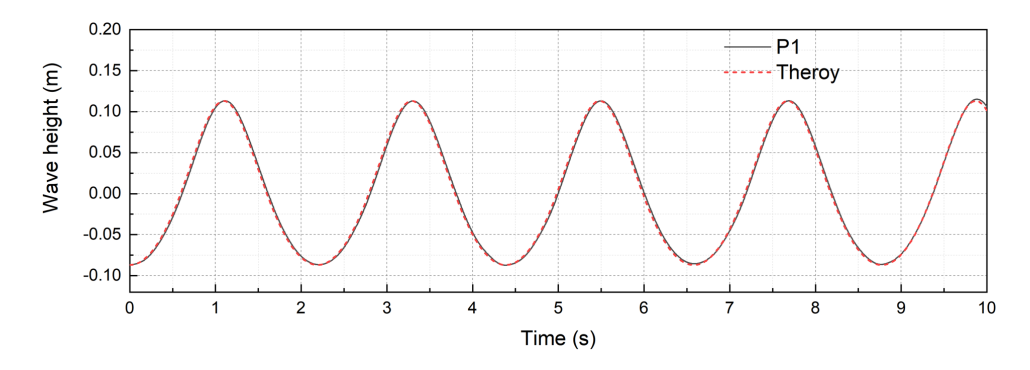


Figure 3 – P1 waveform time history curve

#### 3.2 Verification of the standard model of vortex excitation of elastic plate

In order to verify the reliability of the implicit bidirectional fluid-structure coupling algorithm adopted in this paper, this chapter selects the standard example of vortex-induced fluid-structure coupling of a square head elastic plate [11][12] for verification. The calculation model is shown in Figure 3.3. An elastic cantilever plate is fixed on a cube block with a side length of 1 cm. The boundary conditions are shown in the figure. The left side and the upper and lower boundaries are velocity inlets, and the incoming flow velocity is 0.513 m/s along the x direction; the right side is a zero pressure outlet; the front and rear surfaces are symmetry planes, and only one layer of grid is generated along the y direction to ensure the quasi-two-dimensional characteristics of the flow.

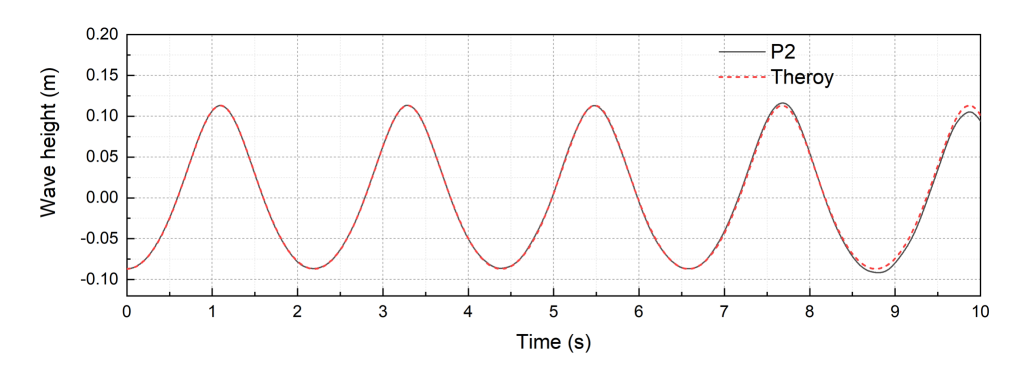


Figure 4 – P2 waveform time history curve

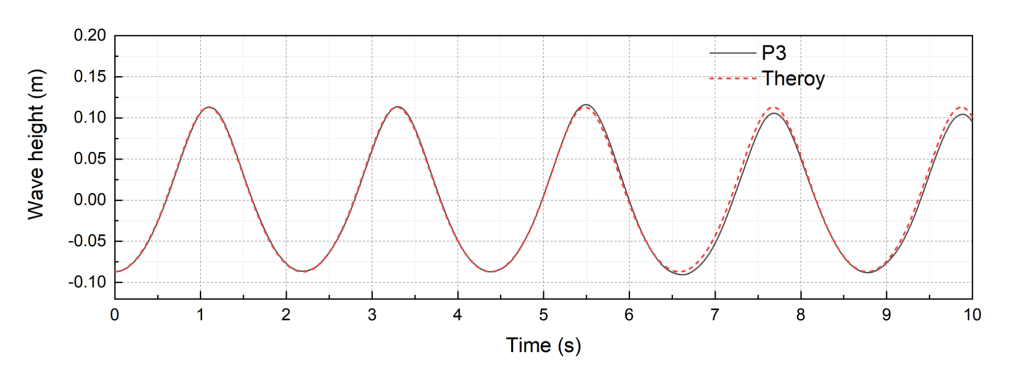


Figure 5 – P3 waveform time history curve

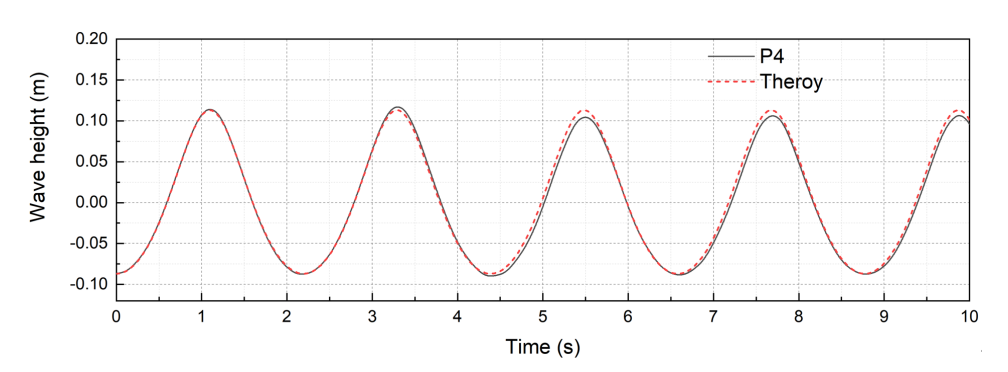


Figure 6 – P4 waveform time history curve

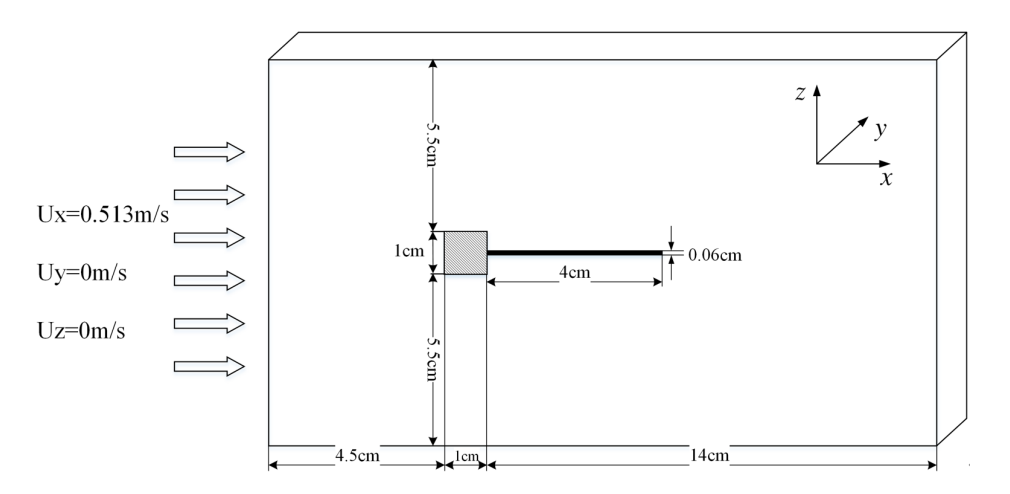


Figure 7 – Computational model of vortex excitation of elastic plate

Figure 8 is a vortex cloud diagram of the flow field during the vortex-induced vibration of the elastic plate. It can be seen that the vibration of the elastic plate is closely coupled with the vortex in the flow

field. Figure 9 shows the comparison between the numerical calculation results based on the above two grid strategies and the results of Liu Y [13].

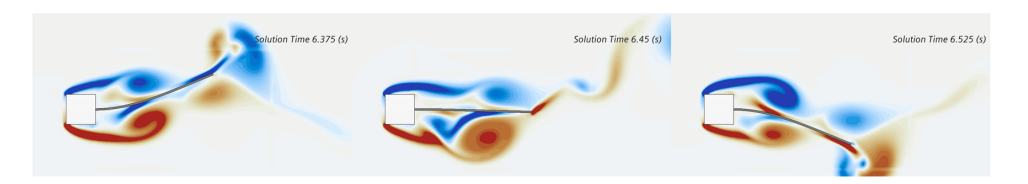


Figure 8 – Vorticity cloud diagram of vortex-induced vibration of elastic plate

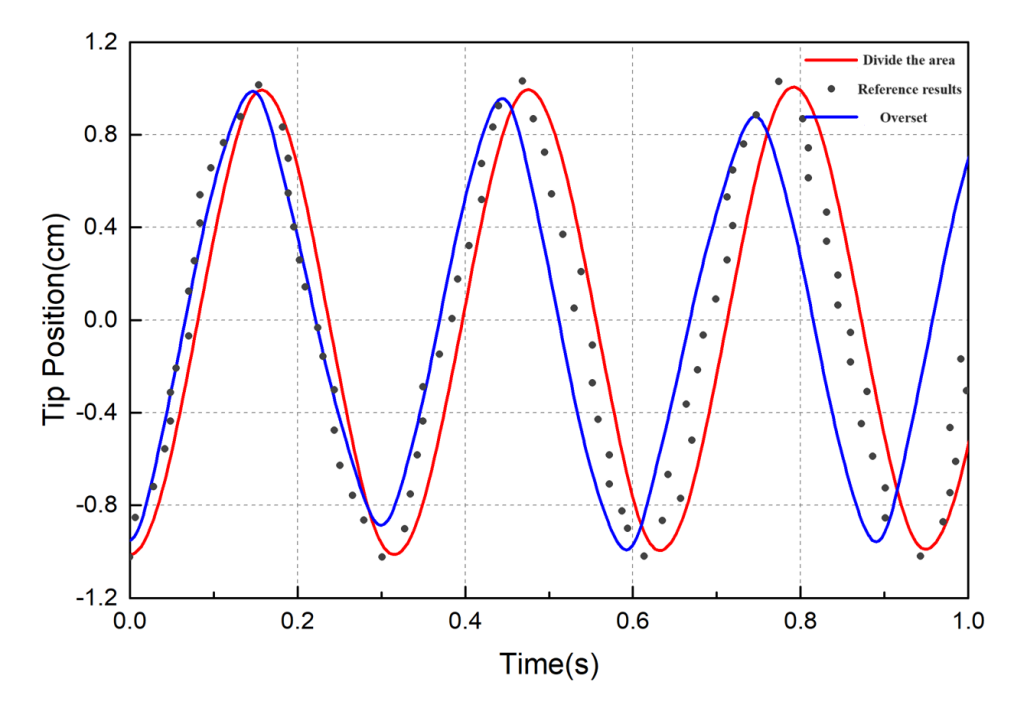


Figure 9 – Comparison of calculation results between the region partition method and the overlay grid method

Compare to the comparison results, whether the regional division method or the overlapping grid method is used, the numerical calculation results of this paper are similar to the research results of other scholars, proving that the implicit bidirectional fluid-solid coupling algorithm used in this paper has good reliability.

### 4. Study on the Structural Response of Seaplane Wing during planing

## 4.1 Simulation Model

The body and computational domain grids are shown in Figure 10. Due to the symmetry of the flow field, the computational model in this paper uniformly adopts half-model calculation. The peripheral flow field adopts Cartesian grid. The vibration of the aircraft wing will cause the mesh to deform in the form of stretching or compression. The deformation and reconstruction of the mesh needs to be calculated at each time step, and the flow field flux needs to be processed according to the changes in the mesh. Therefore, if the global mesh is set to be deformable, it will cause a waste of computing resources. In order to reduce the amount of calculation for mesh reconstruction caused by wing deformation, a flow field domain is separately divided in the flow field around the wing, as shown in the red area in Figure 10. The mesh deformation and reconstruction is only performed in a small area, and the mesh of the peripheral flow field maintains rigid motion. The boundary condition setting is shown in Figure 10, which consists of four velocity inlets, one pressure outlet, and one symmetry surface.

The structural response of the wing is solved based on Simcenter STAR-CCM+ finite element solid stress module. Since only hexahedral meshes and tetrahedral meshes are supported, considering

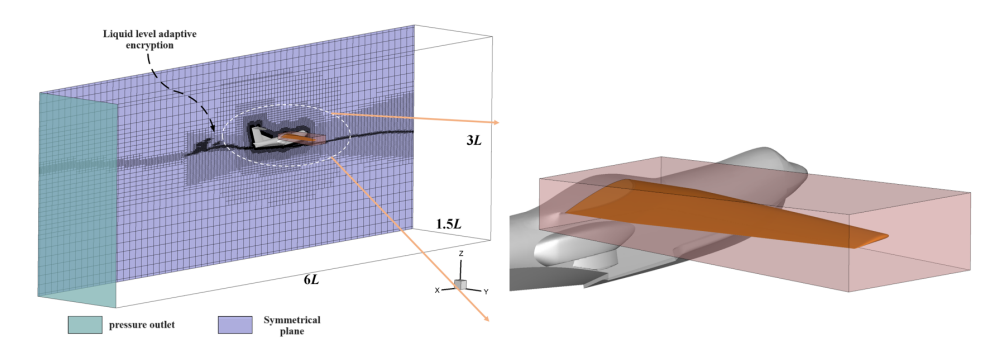


Figure 10 – Comparison of calculation results between the region partition method and the overlay grid method

the relatively complex structure of the wing, this paper uses tetrahedral meshes to discretize the wing. In the Figure 11 mesh size is about 0.01m.



Figure 11 – Wing solid domain mesh

### 4.2 Effects of different planing speeds on aircraft motion and wing structural response

This study analyzes the effects of different gliding speeds on the overall gliding motion state of the aircraft and the wing structure response when the seaplane glides on the high sea wave surface. The wave elements are: fifth-order Stokes wave, wave height 2 meters, wavelength 100 meters. The gliding speeds of the aircraft are 12.64m/s, 18.97m/s, 25.3m/s, and 31.6m/s respectively. The initial position of the aircraft is at the wave down wave position.

Figure 12 and 13 shows the heave displacement time history curve of the aircraft center of gravity at different speeds, as well as the lowest point, highest point and heave motion amplitude of the aircraft center of gravity at each speed. As the planing speed increases, the frequency of encountering waves increases, and the vertical motion response frequency of the aircraft also increases. The increase in the aircraft planing speed causes the hydrodynamic lift and aerodynamic lift on the aircraft to increase, causing the lowest and highest points of the aircraft's heave displacement to move upward during the planing process. However, when the aircraft planing speed reaches 25.3m/s, the highest point of the aircraft's heave displacement decreases with the speed increase, and the lowest point increases with the speed increase, which eventually leads to a gradual decrease in the amplitude of the aircraft's heave motion. It can be seen that during the aircraft's planing on the water surface in high sea conditions, the heave displacement amplitude will reach a peak at 25.3m/s, and then the aircraft's heave motion will tend to be flat until the aircraft takes off.

Figure 14 and 15 shows the time history curve of the aircraft's longitudinal tilt angle change at different planing speeds, as well as the range and amplitude of the aircraft's pitch angle change. Compared with the heave displacement, the change of the aircraft's longitudinal tilt angle under the influence of

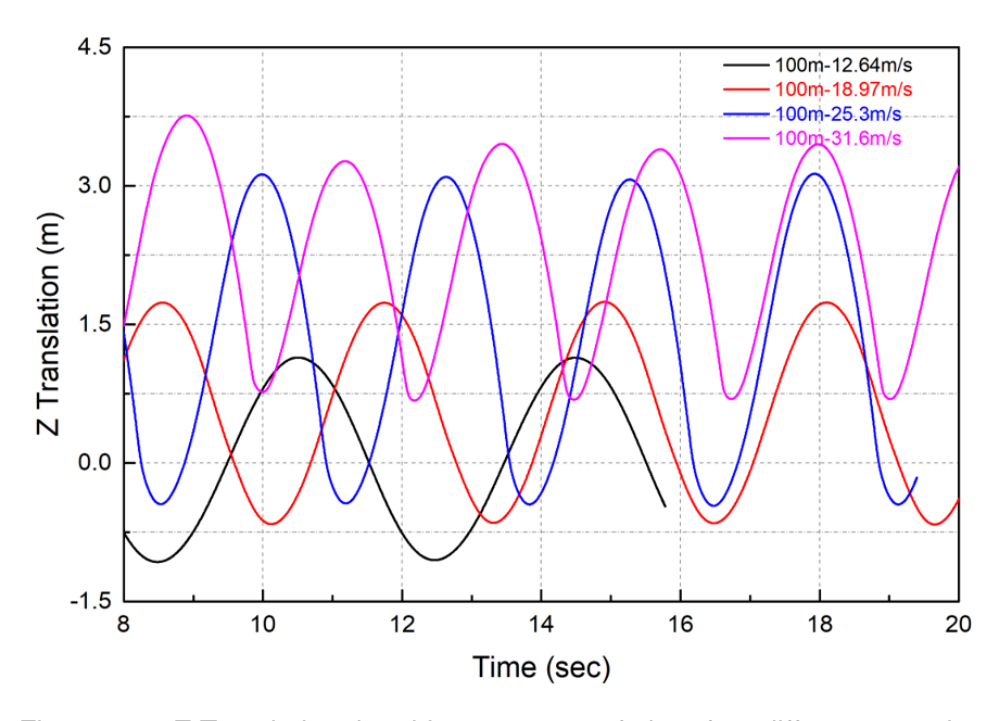


Figure 12 – Z Translation time history curves of aircraft at different speeds

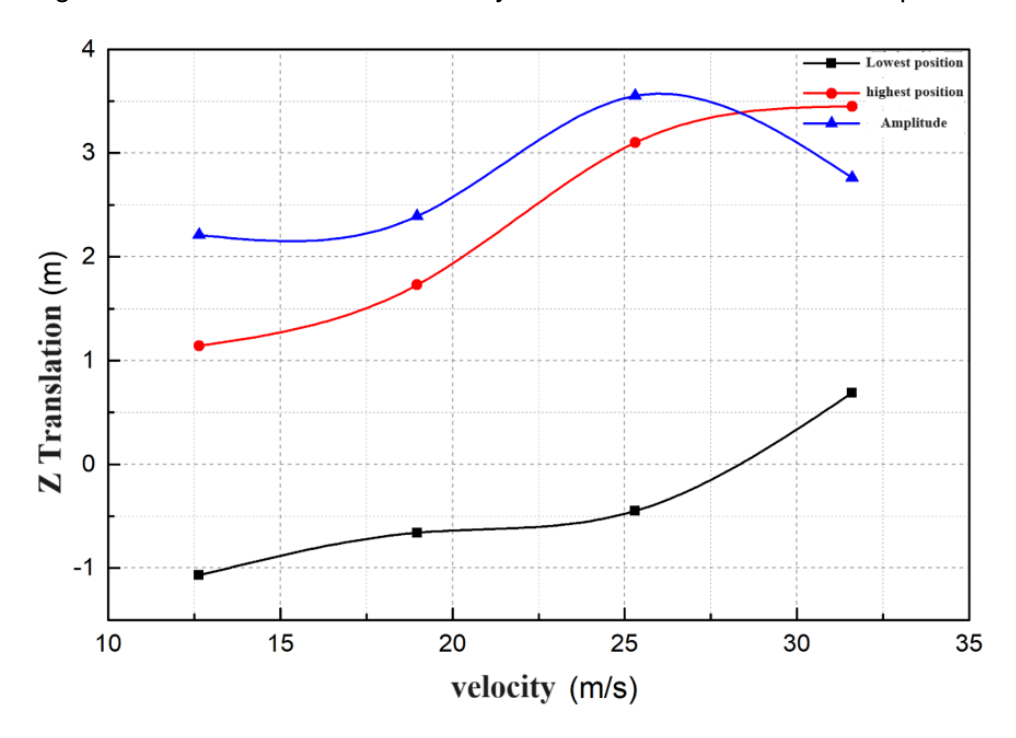


Figure 13 – Range and amplitude of Z Translation of aircraft at different speeds

speed shows a very similar law to the heave displacement. This law is jointly determined by water and aerodynamic forces, as well as the relative position of the aircraft's motion trajectory and the wave surface.

The vertical overload time history curve and range of the aircraft during planing are shown in Figure 16-17. As can be seen from the figure, the overload of the aircraft during planing roughly presents three different forms. When the speed is low, the aircraft always maintains stable planing on the water surface, and the vertical overload of the aircraft is very gentle at this time; when the speed increases to 18.97m/s, the vertical overload of the aircraft will have two peaks of similar size. This is because the front part of the aircraft will leave the water after passing the wave crest, and then as the center of gravity of the aircraft decreases and the head moves down, the front part of the aircraft will hit the downward position of the wave, which leads to the first peak on the overload curve. Then the

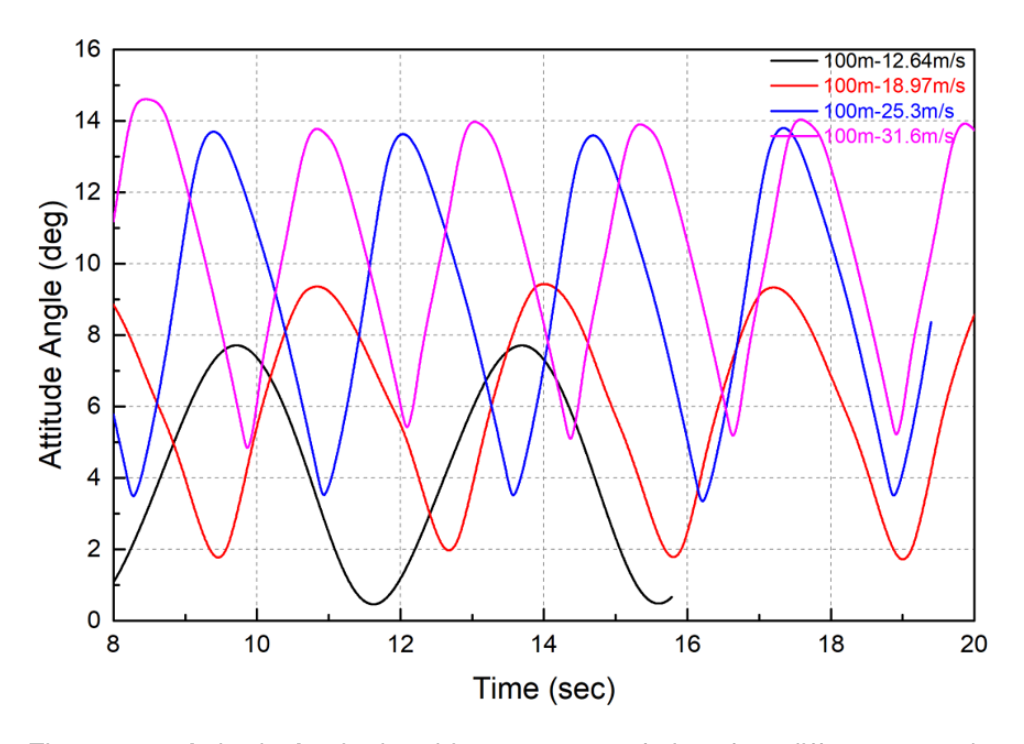


Figure 14 – Attitude Angle time history curves of aircraft at different speeds

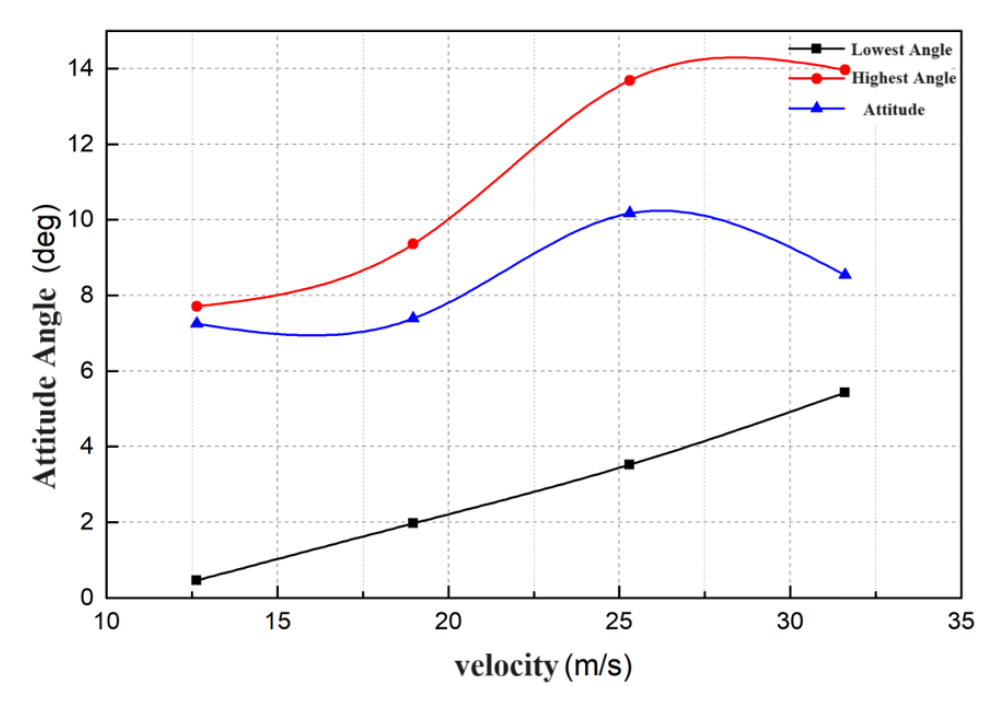


Figure 15 – Range and amplitude of Attitude Angle of aircraft at different speeds

aircraft slides to the trough and encounters the upward position of the next wave, thus generating the second peak; as the planing speed of the aircraft continues to increase, the overload of the aircraft will form a third form, that is, a very large peak appears on the curve. As can be seen from Figure 17, the minimum overload value of the aircraft during planing first decreases slightly with the speed, and increases after reaching 25.3m/s. The main reason for this phenomenon is that the increase in aircraft speed leads to a decrease in the hydrodynamic force after passing the wave crest, while the aerodynamic force as compensation is limited, which leads to a continuous decrease in the minimum overload. When the speed exceeds 25.3m/s, the aircraft will completely leave the water after passing the wave crest. At this time, the vertical overload of the aircraft will be completely determined by the aerodynamic load on the aircraft.

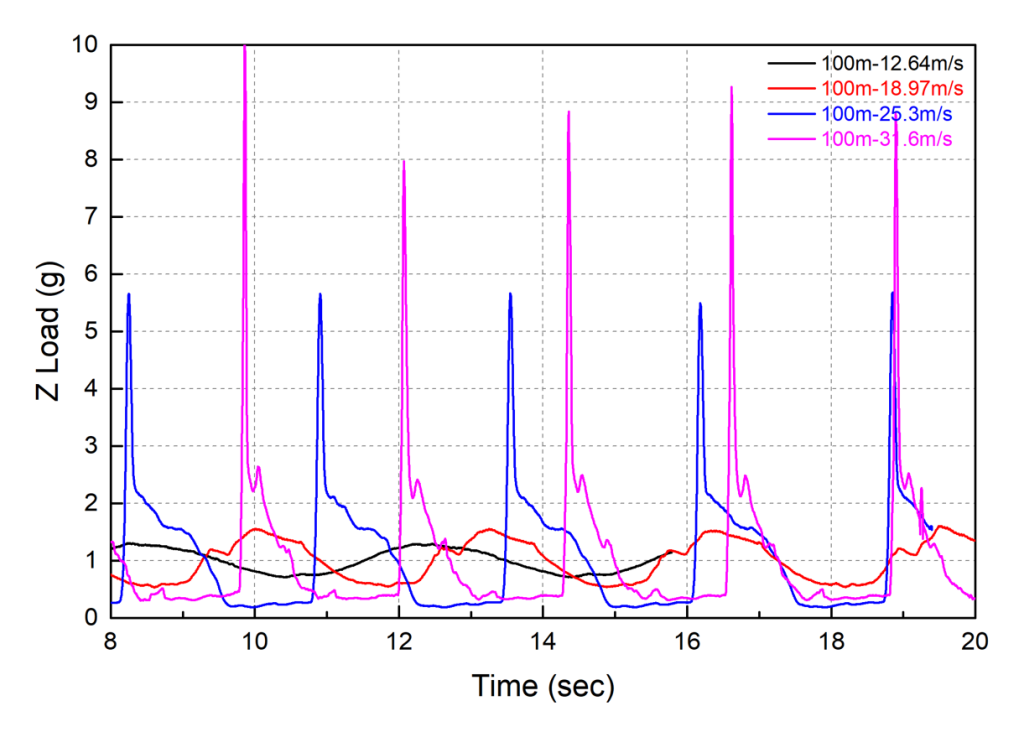


Figure 16 – Vertical overload time history curves at different speeds

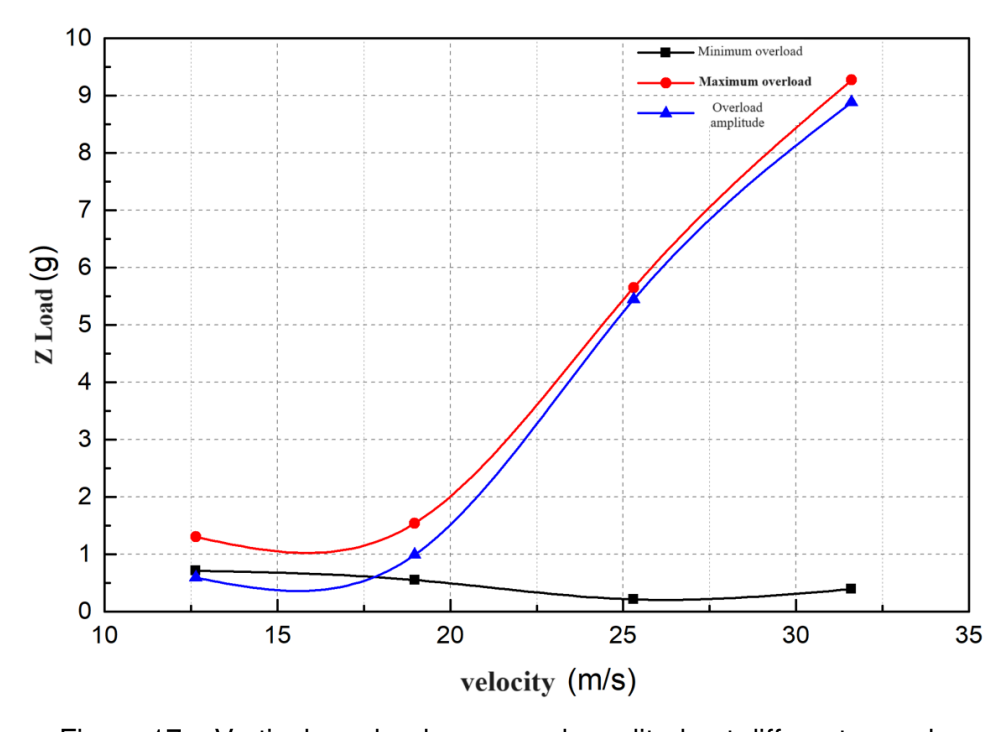


Figure 17 – Vertical overload range and amplitude at different speeds

Figure 18 shows the range of the bending moment at the wing root at different planing speeds, and Figure 19 shows the range of the wing tip vibration at different planing speeds. Comparing the two, it can be seen that they show a very obvious correlation, and the swing range of the wing tip is positively correlated with the wing root bending moment. This is in line with common sense. In addition, with the increase of speed, the wing root bending moment and the wing vibration range experience three stages: gentle growth-rapid growth-slow growth. The occurrence of this phenomenon is closely related to the vertical overload of the aircraft. As mentioned above, at different planing speeds, the vertical load of the aircraft has three different forms, namely, small-amplitude stable changes, small-amplitude double peaks, and large overload peak loads. The first two load forms correspond to the first stage of stable growth of the bending moment and wing tip vibration; the second load form

changes to the third load form, causing the rapid growth of the wing root bending moment and wing tip vibration; then, the load form remains unchanged, but the peak value increases, corresponding to the second stage of slow growth of the bending moment and wing tip vibration.

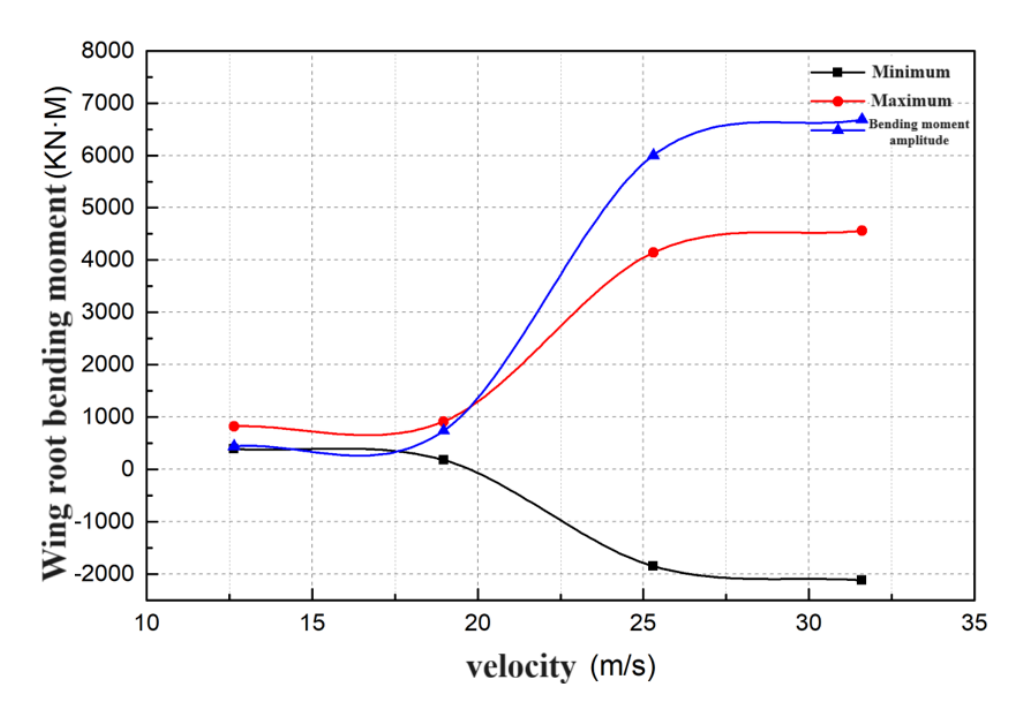


Figure 18 – Variation range of wing root bending moment at different speeds

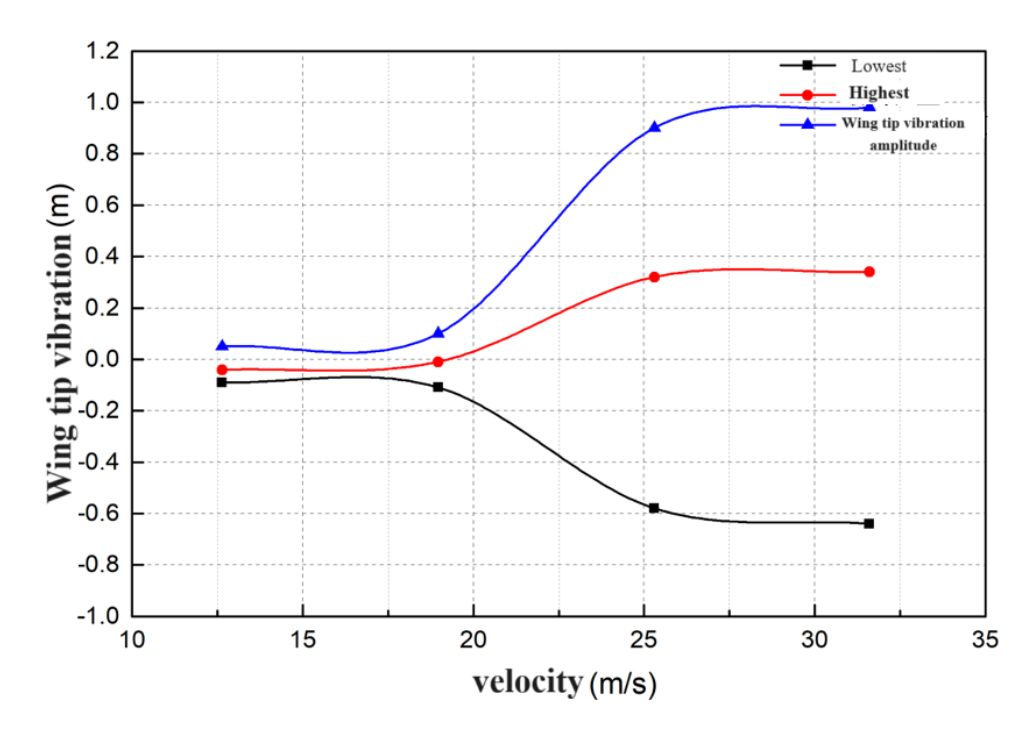


Figure 19 – Wing tip vibration range at different speeds

### 5. Conclusion

The working conditions of different planing speeds were calculated and analyzed. It was found that as the planing speed increases, the frequency of wave encounter increases, and the response frequency of aircraft movement also increases accordingly. The heave displacement and pitch angle amplitude of the aircraft first increase and then decrease with the planing speed; the vertical overload time history curve shows three different forms as the speed increases; the aircraft wing structure

response, including the vibration of the wing tip and the bending moment of the wing root, has a significant correlation with the overload of the aircraft during planing. When the planing speed is low, the overload is small, and it changes smoothly like a simple harmonic curve. The wing tip vibration and wing root bending moment time history curves also roughly show the characteristics of a simple harmonic curve. When the planing speed is high, a large slamming overload will occur at this time, and the wing tip vibration and wing root bending moment time history curves will show a violent oscillation-gradually attenuated response form.

## 6. Acknowledge

This work was supported by Aeronautical Science Foundation of China (No.20230023052001) and Aeronautical Science Foundation of China (No.20220023052001). The authors acknowledge the resources provided by Nanjing University of Aeronautics and Astronautics HPC.

Mail to: luzw0820@163.com

## 7. Copyright Statement

The authors confirm that they, and/or their company or organization, hold copyright on all of the original material included in this paper. The authors also confirm that they have obtained permission, from the copyright holder of any third party material included in this paper, to publish it as part of their paper. The authors confirm that they give permission, or have obtained permission from the copyright holder of this paper, for the publication and distribution of this paper as part of the ICAS proceedings or as individual off-prints from the proceedings.

#### References

- [1] Shao W.B., Ma S and Duan W.Y. Calculation of still water resistance of planing boat based on CFD technology. *Ship Engineering*. v.41;No.271(09):49-53+145, 2019.
- [2] Cai YF, Wang L.L. and Jiang R. Computational fluid dynamics based gliding process of tandem-wing amphibious aircraft on static water surface. *System Simulation Technology*. 14(04):78-83, 2018.
- [3] Duan X.P., Sun W.P. and Wei M. Research on high-speed gliding of amphibious aircraft on water surface based on OpenFOAM. *HANGKONG XUEBAO*. 040(001):136-149, 2019.
- [4] Zhao Y.K., Sun WP and Wei M. Numerical study on mechanical characteristics of seaplane during the whole process of landing on water. *Journal of Beijing University of Aeronautics and Astronautics*. 040(001):136-149, 2019.
- [5] De Marco A, Mancini S, Miranda S, et al. Experimental and numerical hydrodynamic analysis of a stepped planing hull. *Applied Ocean Research*. 64: 135-154, 2017.
- [6] Garland W R, Maki K J. A numerical study of a two-dimensional stepped planing surface. *Journal of Ship Production and Design*. 28(2): 60-72, 2012.
- [7] Matveev K I. Two-dimensional modeling of stepped planing hulls with open and pressurized air cavities. *International Journal of Naval Architecture and Ocean Engineering.* 4(2): 162-171, 2012.
- [8] Matveev K I. Hydrodynamic modeling of semi-planing hulls with air cavities. *International Journal of Naval Architecture and Ocean Engineering*. 7(3): 500-508, 2015.
- [9] P. Lotfi, M. Ashrafizaadeh, R.K. Esfahan. Numerical investigation of a stepped planing hull in calm water *Ocean Eng.* 7(3): 94 103-110, 2015.
- [10] Stern F, Yang J, Wang Z, et al. Computational ship hydrodynamics: Nowadays and way forward. *International Shipbuilding Progress*. 60(1-4): 3-105, 2013.
- [11] Habchi C, Russeil S, Bougeard D, et al. Partitioned solver for strongly coupled fluid–structure interaction. *Computers and Fluids*. 60(1-4): 3-105, 2013.
- [12] Wood C, Gil A J, Hassan O, et al. Partitioned block-Gauss-Seidel coupling for dynamic fluid-structure interaction. *Computers and structures*. 60(1-4): 3-105, 2013.
- [13] Liu Y, Xiao Q, Incecik A. A coupled CFD/multibody dynamics analysis tool for offshore wind turbines with aeroelastic blades. *International Conference on Offshore Mechanics and Arctic Engineering*. 57786: V010T09A038, 2017.